Journal of
Materials Chemistry A
Materials for energy and sustainability

This article can be cited before page numbers have been issued, to do this please use: X. Wang, J. Zhang, X. Li, H. Yu, L. Tan, Q. Wang, W. Xu, B. Xu, S. Xiao and J. Huang, *J. Mater. Chem. A*, 2025, DOI: 10.1039/D5TA03812J.

View Article Online
DOI: 10.1039/D5TA03812J

A facile strategy to design shape memory rubber composites with tunable mechanical properties and photothermal performance

Xiao Wang[1,2], Jiahui Zhang[1,2], Xiaoting Li[1,2], Huiwen Yu[1,2], Lingcao Tan[1,2],
Qiongyao Wang[1,2], Wenhua Xu[1,2,3], Baiping Xu[1,2], Shuping Xiao[1,2,], Jiarong Huang[1,2,*]*

1. School of Mechanical and Automation Engineering, Wuyi University, Jiangmen, 529020, China.

2. Jiangmen Key Laboratory of Polymer Intelligent Manufacturing (Wuyi University), Jiangmen, 529020, China.

3. Guangdong Provincial Key Laboratory of Technique and Equipment for Macromolecular Advanced Manufacturing, South China University of Technology, Guangzhou, 510640, China.

Corresponding Author: Jiarong Huang (hjr@wyu.edu.cn), Shuping Xiao (xsp@wyu.edu.cn)

Abstract: Shape memory polymers (SMPs) represent a prominent category of smart polymers that show attractive prospects in emerging fields of soft robots and biomedical devices. However, most of the existing SMPs show limitations in single-stimulus responsiveness and an imbalance between mechanical and shape memory properties. Herein, biological phytic acid served as a natural curing agent to vulcanize the biobased epoxidized natural rubber (ENR), while Fe^{3+} was introduced to construct a second cross-linked network based on coordination interaction. Polycaprolactone (PCL) was introduced and acted as net points to regulate the shape fixing behavior, while the dual cross-linked network provided strong resilience to achieve the shape recovery performance. Meanwhile, the Fe^{3+}-based coordination complex not only served as sacrificial elements to realize tunable mechanical properties by effectively dissipating energy, but also acted as a photothermal agent to realize the light-induced shape memory behavior and thermoelectric power generation. The fabricated composites process multi-stimuli-responsive shape memory properties, photothermal capabilities, and tunable mechanical properties, exhibiting outstanding potential in harvesting sunlight for outdoor portable power generation and stimuli-responsive sensors.

Keywords: Epoxidized natural rubber, Dual cross-linked networks, Multi-stimuli-responsive shape memory, Photothermal effect

1. Introduction

Shape memory polymers (SMPs) are stimulus-responsive materials that can be deformed to obtain a temporary shape and then recover their original shape when subjected to an external stimulus, such as light, heat, electricity, magnetism, and so on[1-4]. In recent years, SMPs have developed rapidly

View Article Online
DOI: 10.1039/D5TA03812J

due to their advantages of being lightweight, cost-effective, and capable of fast response and wide response strain[5,6]. Therefore, SMPs have become one of the primary directions in the development of new, modern high-tech materials that integrate sensing, actuation, information processing, and autonomous deformation.

Various strategies have been proposed to fabricate SMPs, such as the construction of a glassy transition gradient, rubber/plastic blending, and the construction of an interpenetrating network[7-13]. Among these methods, rubber/plastic blending is considered one of the most facile strategies to endow polymers with a shape memory effect[14-18]. On the one hand, the plastic component can act as net-points to fix the temporary shape, improving the shape memory effect. On the other hand, the plastic component exhibits excellent thermoplasticity, providing the covalently cross-linked rubber with processability. Xu et al. prepared ethylene propylene diene monomer/polypropylene thermoplastic vulcanizate (PP/EPDM TPV) with a sea-island structure through dynamic vulcanization, in which the PP matrix could maintain the temporary shape of TPVs and the cross-linked EPDM phase supplied stress to drive the deformed shape recovery during the shape memory process[19]. We have fabricated a series of shape memory polylactic (PLA)/rubber blends, in which the continuous PLA matrix acted as a controlling switch to fix/release the programmed shapes, and the rubber network drove the recovery of the permanent shape[20,21]. However, the shape memory effect of rubber-based SMPs essentially stems from the entropic elasticity of rubber[22], which needs to be triggered by temperature. Therefore, most of the existing rubber-based SMPs are heat-triggered SMPs, which are limited to responding to a single stimulus, hindering their future application in the realm of smart materials.

To overcome the above restriction, various functional fillers have been utilized to fabricate multi-stimuli-responsive SMPs, whose shape memory effect can be triggered by light, moisture, electrical/magnetic fields, and so on[23-26]. Among all stimulus-triggered SMPs, light-triggered SMPs have attracted much attention due to their excellent characteristic of remote activation and spatial controllability. The light-responsive capacity can be introduced to SMPs by two different mechanisms. The first is achieved via integrating intrinsic light-responsive molecular units into the matrix, while the second mechanism utilizes photothermal effects. Various fillers, such as graphene, carbon nanotubes, melanin, gold nanomaterials, and metal ion-based coordination compounds, can be used as photothermal agents to introduce the photothermal effect into the matrix[20,27-29]. However, the introduction of functional fillers is often accompanied by a deterioration in mechanical properties,

View Article Online
DOI: 10.1039/D5TA03812J

which is caused by the poor compatibility and aggregation of the fillers[30,31]. Generally speaking, interface modification can improve compatibility. However, such improvement is always accompanied by a large amount of additional modification work and extensive use of chemical reagents, and there is a possibility that the functional properties of the filler may be lost. Therefore, there remains a critical demand for designing shape memory composites that encompass tunable mechanical properties and multi-stimuli responsiveness.

Inspired by the hierarchical architectures in natural materials, various energy-dissipating strategies, such as weak interactions, dual/multi-cross-linked networks, and heterogeneous domains, have been introduced to improve the mechanical properties of rubber-based materials[32-35]. Ducrot et al. synthesized tough elastomers consisting of a rigid network and a flexible second network, where the rigid network could be preferentially broken to dissipate energy, leading to toughening of the elastomers[32]. Guo et al. fabricated a mechanically robust styrene-butadiene rubber (SBR) by introducing polysulfide to achieve the chemical cross-linking of SBR and grafting iron-carboxylate complexes onto SBR chains[33]. The grafted iron-carboxylate complexes aggregated to form a phase-separated structure, which enhanced the mechanical properties by promoting energy-dissipating efficiency. Inspired by the current research, in this work, we intend to design a shape memory elastomer by introducing Fe^{3+}-based coordination compounds into the rubber/plastic system, in which the coordination compounds not only act as the photothermal agent to realize light-triggered shape memory behavior, but also act as a second cross-linked network to reinforce the composites.

Here, we present a facile and effective strategy to prepare shape memory composites with tunable mechanical properties and shape memory capabilities simultaneously. Polycaprolactone (PCL) was introduced into the ENR matrix to regulate the shape fixing behavior of ENR based on the glassy state of PCL at 25 °C, and release the temporary shapes based on the melting behavior of PCL at ~60 °C. Phytic acid, a natural plant product, was utilized as a curing agent to cross-link ENR based on esterification reactions between phosphate groups and epoxy groups[31,36]. Subsequently, Fe^{3+} ions were utilized to construct the second cross-linked network through the coordination interaction between Fe^{3+} and oxygen-containing groups. On the one hand, the dual cross-linked network could construct a tunable glass transition gradient, which would help improve the shape memory performance. On the other hand, the coordination bonds serve as sacrificial elements to promote the dissipation of energy when subjected to external force, achieving the remarkable reinforcement of the composites. Additionally, the coordination compounds based on Fe^{3+} are available as photothermal

View Article Online
DOI: 10.1039/D5TA03812J

agents because of their excellent photothermal effect, expanding the shape memory capabilities and thermoelectric power generation under near-infrared light or sun irradiation.

2. Experimental section

2.1. Materials

Epoxidized natural rubber (ENR) with an epoxidation degree of 50% was supplied by the Chinese Academy of Tropical Agricultural Sciences. Polycaprolactone (PCL, Capa 6500) with M_n =80000 g/mol was purchased from Perstorp (Sweden). Phytic acid (PA) solution (50 % in H_2O) was purchased from Shanghai Aladdin Bio-Chem Technology Co., Ltd., where PA was dehydrated before use. Iron chloride hexahydrate ($FeCl_3 \cdot 6H_2O$, analytically pure) was purchased from Fuchen (Tianjin) Chemical Reagent Co., Ltd. (China).

2.2 Sample preparation

The ENR/PCL blends with different ENR/PCL ratios were obtained through a torque rheometer (RTOI-06/02, POTOP, China) at 80 ℃ with a rotor speed of 60 rpm, and then the ENR/PCL blends with a thickness of 1 mm were compression moulded at 170 °C and 5 MPa for 5 min. The corresponding formulations are listed in Table S1. The ENR/PCL blends were named ExPy, where x represented parts of ENR, and y represented parts of PCL.

To eliminate the influence of moisture in PA, the PA aqueous solution was concentrated to remove most of the water, which can be found in the *Supporting Information* section (Figure S1, Figure S2). The ENR/PCL/PA/$FeCl_3$ blends were obtained through a similar process, in which the enriched PA solution and $FeCl_3$ powder were sequentially added to the ENR/PCL blends. Subsequently, the obtained ENR/PCL/PA/$FeCl_3$ blends were compression moulded at 170 ℃ and 5 MPa for 5 min to obtain the composites with a thickness of 1 mm for different tests. Before the compression moulding, the blends were preheated at 170 ℃ for 2 min and then exhausted 8 times, which can help to further remove the residual moisture of PA. The detailed processing technique can be found in the *Supporting Information* section. In the ENR/PCL/PA/$FeCl_3$ composites, the weight ratio of ENR/PCL was fixed at 70/30 (wt.%/wt.%), the loading amount of PA solution was fixed at 0.5 phr (parts per hundred parts) of ENR, and the loading amounts of $FeCl_3$ powder were 0, 0.5, 1, 2, and 3 phr of ENR, respectively. The detailed formulations of ENR/PCL/PA/$FeCl_3$ composites are listed in Table S2. The obtained ENR/PCL/PA/$FeCl_3$ composites were coded as PA0.5Fz, where z represented parts of $FeCl_3$.

View Article Online
DOI: 10.1039/D5TA03812J

2.3 Characterization

The rheological behavior was evaluated at 170 °C through a rotational rheometer (HAAKE MARS 60-Nicolet iS20, Germany). X-ray photoelectron spectroscopy (XPS) was carried out on a Thermo Fisher Scientific Nexsa using hybrid lens mode. The morphology of the tensile-fractured sample was observed through a scanning electron microscope (SEM, Star, Thermo Fisher Scientific, Netherlands). Fourier transform infrared spectroscopy (FTIR) was performed on a Brooke ALPHA FTIR spectrometer in an attenuated total reflectance (ATR) model for pure ENR, ENR/PCL blend, and ENR/PCL/PA/$FeCl_3$ composites. All the spectra were taken from 4000 to 400 cm^{-1}, with a spectral resolution of 4 cm^{-1} and an accumulation of 32 scans. Differential scanning calorimetry (DSC) was conducted on a DSC 3500 (Netzsch, Germany). The DSC tests were conducted from room temperature to 170 °C with a heating rate of 10 °C/min under a nitrogen atmosphere, and kept at 170°C for 10 min to eliminate thermal history. Then, all of the samples were cooled down to -60 °C under 10 °C/min, followed by heating again to 170 °C under 10 °C/min.

Cross-link densities were measured according to equilibrium swelling experiments. In brief, the preweighed specimens were immersed in toluene under a shaded environment, and the swollen samples were periodically taken out from the toluene and weighed immediately. The weight measurements were continued until the swollen samples reached constant values. The cross-link densities were calculated according to the Flory-Rehner equation[37]:

$$\mathrm{V} = -\frac{\ln(1-V_0)+V_0+xV_0^2}{V_1(V_0^{\frac{1}{3}}-\frac{V_0}{2})} \tag{1}$$

where

$$V_0 = \frac{m_2/\rho_2}{m_2/\rho_2+(m_1-m_2)/\rho_1} \tag{2}$$

Where V_1 is the molar volume of toluene (V_1 = 106.2 cm^3 /mol), x is the polymer-solvent interaction parameter (x = 0.3441 for ENR and toluene). ρ_1 (0.865 g/cm^3) and ρ_2 (0.96 g/cm^3) are the densities of toluene and ENR, respectively. m_1 and m_2 are the masses of the swollen sample and the dried sample, respectively.

Dynamic mechanical analysis (DMA) was performed on METTLER DMA 1 under tension mode. The DMA was performed from -70 °C to 80 °C with a heating rate of 3 °C/min and a frequency of 1 Hz. Tensile tests were conducted at room temperature through the CREE-8003D tensile machine (Dongguan CREE INST Rument Technology Co., Ltd, China). The crosshead speed was fixed at 500

View Article Online
DOI: 10.1039/D5TA03812J

mm/min according to ISO 37-2017, and five specimens were tested for each formula to obtain average values.

The multi-stimuli-responsive shape memory properties were evaluated according to Figure S3, which was described in the *Supporting Information* section in detail. During the light-triggered shape memory test, a sun simulator (PLS-SXE300+, Beijing Perfectlight Technology Co., Ltd) and a near-infrared laser (NIR, 808 nm, 0-4 W, HW808AD4000-100F, Shenzhen Infrared Laser Technology Co., Ltd, China) were used as light sources. And the temperature of the sample surface was recorded using an infrared imager (R60, Hangzhou Meisheng Infrared Photoelectric Technology Co., Ltd, China). The photo-thermoelectric generator (PTEG) system consisted of a Seebeck thermoelectric generator (SP1848-27145), a heat sink, and an ENR/PCL/PA/$FeCl_3$ composite film. The temperature of PTEG was recorded using an infrared imager, and the output voltage was recorded with a digital multimeter (Keithley DMM 7510, USA).

3. Results and discussion

3.1 Construction of the dual cross-linked ENR/PCL/PA/$FeCl_3$ composite

Blending with plastic is a facile strategy to endow rubbers with a shape memory effect. However, the simple blending of rubber and plastic will result in inferior mechanical properties[14,15]. To get around this problem, we propose a strategy to fabricate shape memory composites through the following three steps (Figure 1): (1) polycaprolactone (PCL) is introduced into epoxidized natural rubber (ENR) and acts as net points to trigger the shape memory effect; (2) phytic acid (PA) with six phosphate groups is utilized as a biological curing agent to cross-link ENR via the ring-opening reaction between phosphate groups of PA and epoxy groups of ENR, aiming to construct a covalent adaptable network; (3) Fe^{3+} is introduced into the matrix to construct a second cross-linked network based on the coordination interaction between Fe^{3+} and oxygen-containing groups of ENR, which can act as a sacrificial component to improve the mechanical properties.

To verify the above assumption, the rheological behaviors of ENR/PCL blend (E7P3), ENR/PCL/PA blend (PA0.5F0), and ENR/PCL/PA/$FeCl_3$ blend (PA0.5F2) were carried out and are shown in Figure 2a and Figure S4. The viscosity (η) of E7P3 remained almost constant throughout the test time range, while the η of PA0.5F0 increased with time, revealing that PA could realize the vulcanization of ENR without any accelerators or additives. Moreover, the η value of the ENR/PCL system could be further improved by introducing Fe^{3+}, ascribed to the coordination interaction between Fe^{3+} and the oxygen-containing group of ENR.

View Article Online
DOI: 10.1039/D5TA03812J

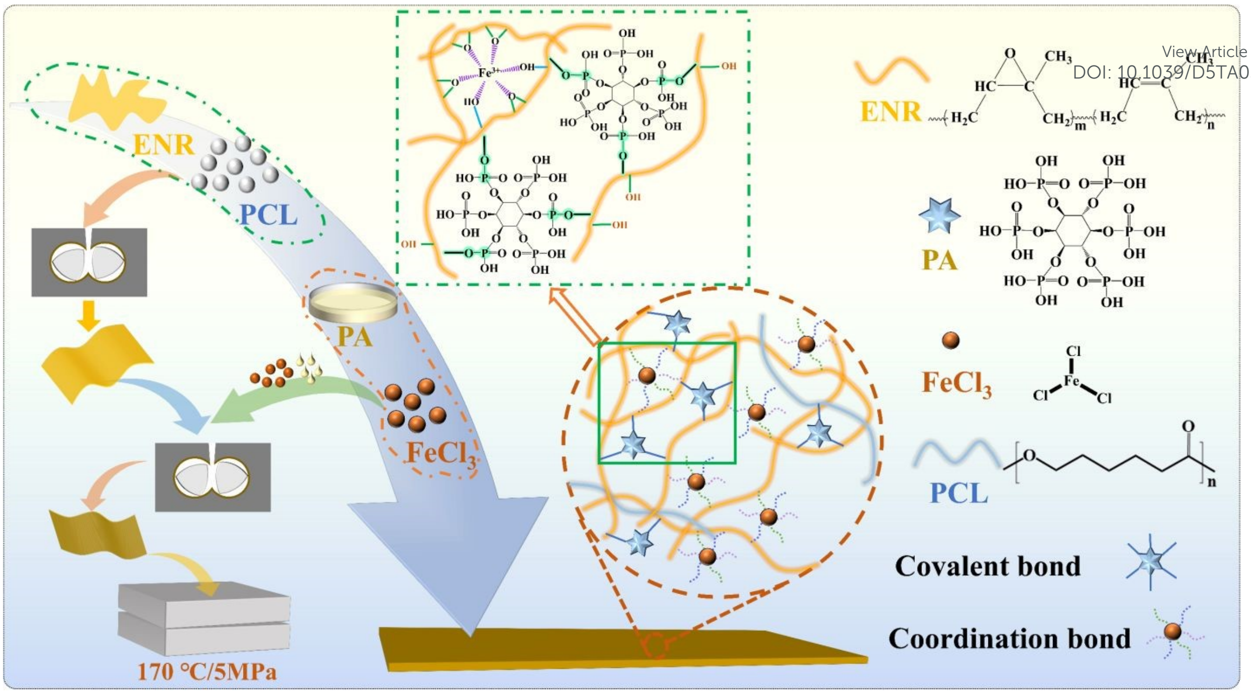

Figure 1. Schematic illustration for preparing ENR/PCL/PA/FeCl$_3$ composite.

To explore the mechanism of the dual cross-linked network, FTIR spectra of pure ENR, E7P3, PA0.5F0, and PA0.5F2 were characterized and shown in Figure 2b. In addition, the enlarged spectra were compared in Figure 2c. The neat ENR shows an absorption peak at 870 cm^{-1}, which is attributed to the epoxy ring[13,31]. The FTIR spectrum of the ENR/PCL simple blend (E7P3) shows absorption peaks at 1720 cm^{-1}, representing the ester groups of PCL (Figure S5)[7]. When PA is introduced into the ENR/PCL system, the intensity of the epoxy peak at 870 cm^{-1} is decreased, demonstrating the ring-opening reaction of ENR. And another obvious peak at 1064 cm^{-1} corresponded to the formation of C-O-P bonds[31,36,38], which was overlapped by the C-O-C bonds of PCL. Meanwhile, a new absorption peak appeared at 3450 cm^{-1}, caused by the formation of hydroxyl groups during the ring-opening reaction[13,20]. According to the FTIR results, the mechanism of the covalent cross-linked network was proposed in Figure 2d. ENR could be cured by PA via the ring-opening of the epoxy group, accompanied by the formation of phosphonate ester bonds.

Subsequently, when Fe^{3+} was introduced into the ENR/PCL/PA system, the absorption peaks of hydroxyl groups shifted to lower wavenumbers, indicating the association between Fe^{3+} and hydroxyl groups. Besides, for the FTIR spectrum of ENR, the peak around 1064 cm^{-1} has been demonstrated to be the stretching vibration of the tetrahydrofuran ring, which is the inevitable by-product of ENR with high epoxy content. And the peak around 1110 cm^{-1} should be ascribed to the tetrahydrofuran ring associated with hydrogen bonds.[39] Interestingly, the hydrogen interaction was disrupted by Fe^{3+}-O coordination, resulting in the merging of the two peaks for the tetrahydrofuran ring into one broad

View Article Online
DOI: 10.1039/D5TA03812J

band at 1064 cm^{-1}. The XPS results provide additional implications for the Fe^{3+}-O coordination interaction (Figure 2e). For PA0.5F0, a peak with a binding energy of 531.78 eV can be observed in the O^{1s} spectra, corresponding to C-O-C or C-O-H.[13] For PA0.5F2, a shoulder peak with a binding energy of 532.88 eV emerges with the introduction of Fe^{3+}. This emerged peak is ascribed to the more electron-deficient oxygen, disclosing the coordination interaction between Fe^{3+} and oxygen-containing groups. Based on the above results, the mechanism of the coordination cross-linked network was proposed in Figure 2d. After the esterification reaction between ENR and PA, the tetrahydrofuran ring, the residual epoxy group, and the generated hydroxyl groups could interact with Fe^{3+} to form a second cross-linked network[40,41]. Thereby, a dual cross-linked network consisting of covalent phosphonate ester bonds and non-covalent coordination interaction was constructed in the ENR/PCL/PA/$FeCl_3$ composites.

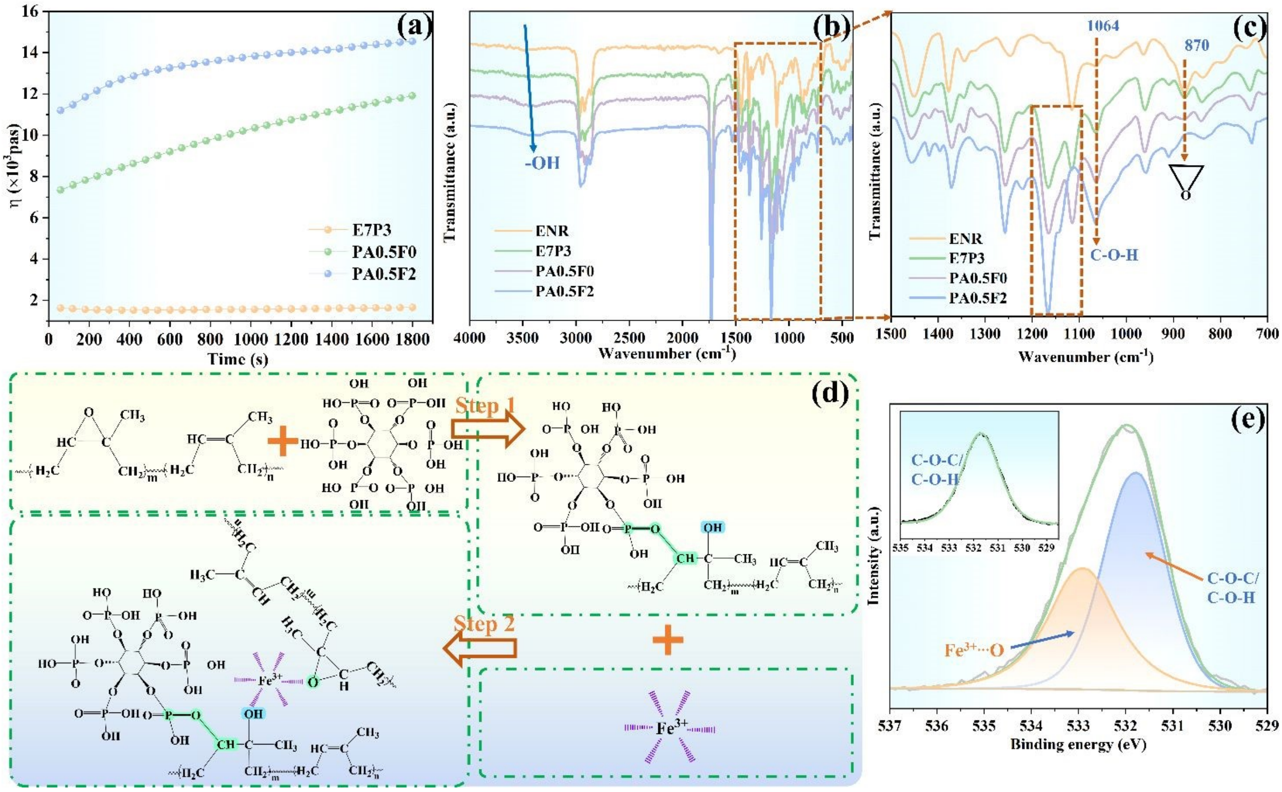

Figure 2. (a) Rheological behaviors of E7P3, PA0.5F0, and PA0.5F2, (b) (c) FTIR spectra of ENR, E7P3, PA0.5F0, and PA0.5F2, (d) the cross-linking mechanism of dual cross-linked network, (e) XPS spectra of PA0.5F0 and PA0.5F2.

Due to the ring-opening reaction between ENR and PA, and the coordination interaction between Fe^{3+} and oxygen-containing groups, many cross-linking centers were formed in the matrix, which could help resist solvent permeation. For the ENR/PCL blend, the PCL component could be dissolved by toluene quickly, and the linear ENR phase of the ENR/PCL blend first became swollen and then

View Article Online
DOI: 10.1039/D5TA03812J

dissolved, resulting in a turbid solution after 60 min (Figure 3a). However, PA0.5F0 exhibited only swelling behavior without dissolution, visually demonstrating the formation of a phosphonate ester-based cross-linked network. Compared with PA0.5F0, PA0.5F2 maintained its integrated shape better after immersing for 5 days, further disclosing the formation of the Fe^{3+}-based coordination complex. Meanwhile, the dried PA0.5F2 gel still maintained its rectangular shape, which could be stretched to a large deformation and then recovered to its original shape, demonstrating that PCL did not break the continuous structure of the ENR matrix.

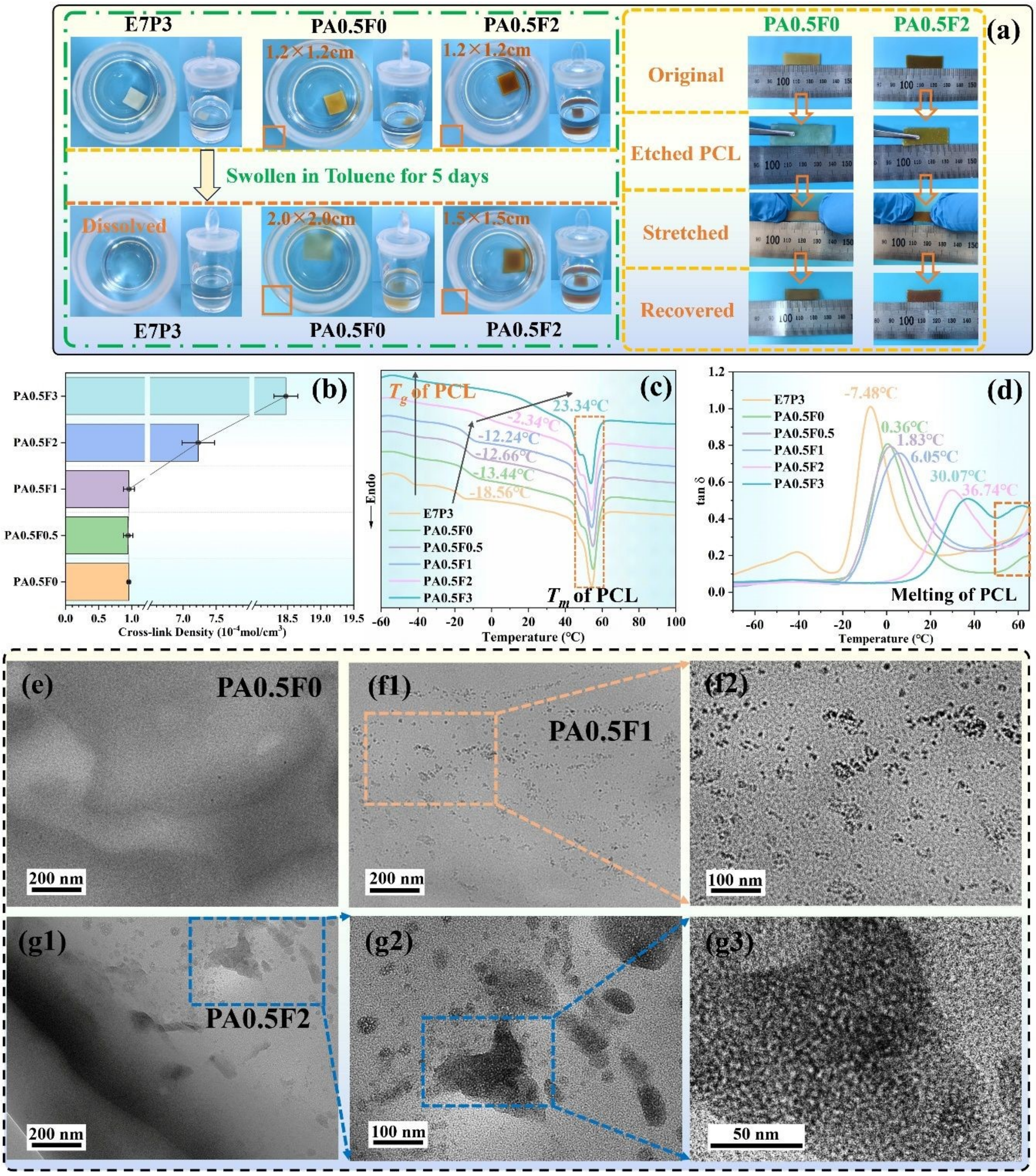

Figure 3. (a) swelling experiments, (b) cross-link densities, (c) DSC curves and (d) DMA curves of the ENR/PCL/PA/$FeCl_3$ composites, TEM images: (e) PA0.5F0, (f) PA0.5F1, (g) PA0.5F2.

Based on the above swelling experiment, the cross-link densities of the ENR/PCL/PA/$FeCl_3$

View Article Online
DOI: 10.1039/D5TA03812J

composites were calculated and shown in Figure 3b. An improved cross-link density was observed with increasing Fe^{3+} content. With the incorporation of 3 phr Fe^{3+}, the cross-link density of the composites (PA0.5F3) reached 18.48 × 10^{-4} mol/cm^3, nearly 19.37 times that of PA0.5F0. The increased cross-link density effectively revealed the consistently developed network architecture, which made it difficult for the solvent to permeate into the matrix.

The increased cross-link density indicates the restricted mobility of the ENR chains, which is consistent with the change in glass transition temperature (T_g), as shown in the DSC curves. As shown in Figure 3c, the platform around -46 ℃ and the peak around 45-60 ℃ represent the glass transition and the melting behavior of the PCL phase, respectively. For the ENR phase, its T_g value increased from -18.56 ℃ of the ENR/PCL simple blends to -13.44 ℃ of PA0.5F0 with the incorporation of PA, because the phosphonate ester-based cross-linked network would make chain segmental motion more challenging and demand more energy to activate. The T_g values could be further improved with increasing Fe^{3+} content. As shown in the DMA curves (Figure 3d), increased T_g values and decreased $tan\delta$ peak values were also observed with increasing Fe^{3+} content, revealing the further restricted mobility of rubber chains due to the higher cross-link density of the composites with higher Fe^{3+} content. Additionally, the last rising areas of the DMA curves were ascribed to the melting behavior of the PCL phase (Figure S6).

TEM tests were carried out for the ENR/PCL/PA/$FeCl_3$ composites to analyze the structure of the composites and the distribution of $FeCl_3$, as shown in Figure 3e, f, and g. For PA0.5F0, the light phase is considered the PCL phase, while the dark phase is the ENR phase, which is consistent with the ENR/PCL ratio. When incorporating $FeCl_3$, the interface between the ENR phase and the PCL phase gradually becomes blurred, which is caused by the migration of Fe^{3+} within the ENR and PCL phases with the help of high temperature and shear force. The black dots in PA0.5F1 are $FeCl_3$, which are uniformly distributed in the matrix (Figure 3f1). Interestingly, a distinct phase-separated structure can be observed in PA0.5F2 (Figure 3g). The darker regions represent the dispersed phase, which is overlapped by many loosely packed spherical-shaped domains with diameters of tens of nanometers. With the increase of Fe^{3+} content, individual coordination bonds within the ENR/PCL matrix aggregate to form segregated phases, which is similar to the formation of ion clusters[29,33].

3.2 Tunable mechanical properties of the composite

Compared to pure ENR with poor mechanical properties, the introduction of PCL reinforces the ENR phase (Figure S7). However, the unvulcanized ENR phase in the ENR/PCL simple blend still

View Article Online
DOI: 10.1039/D5TA03812J

acts as a vulnerable spot, and the mechanical properties of the ENR/PCL simple blend cannot meet most practical applications. To overcome this drawback, a dual cross-linked network was constructed to improve the mechanical properties. The tensile behavior of the ENR/PCL/PA/$FeCl_3$ composites was carried out, and the typical stress-strain curves are presented in Figure 4a. When incorporating PA as a curing agent, a cross-linked network based on phosphonate ester bonds was successfully established in the matrix, improving the mechanical properties of the ENR/PCL/PA elastomer. With 0.5 phr PA, the tensile strength and stress at 100 % strain of PA0.5F0 increased to 7.66 MPa and 1.60 MPa, which are 3.72 times and 3.40 times greater than those of the ENR/PCL simple blend (Figure S8).

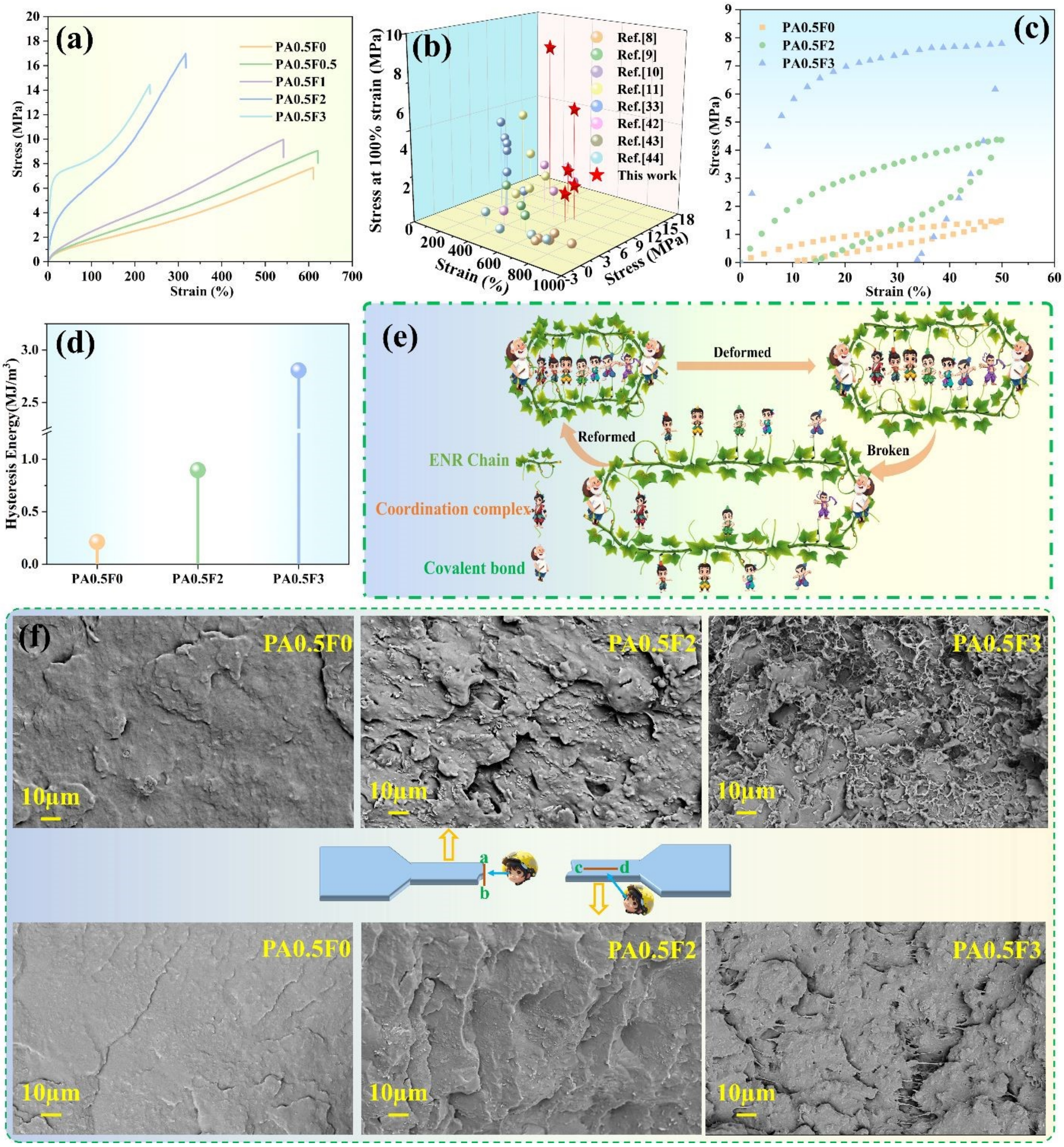

Figure 4. (a) Stress-strain curves of the ENR/PCL/PA/$FeCl_3$ composites, (b) comparison of the

DOI: 10.1039/D5TA03812J

performances of ENR-based composites, (c) loading-unloading cycles and (d) hysteresis energy of PA0.5F0, PA0.5F2 and PA0.5F3 at 50% strain, (e) schematic diagram of the energy-dissipation mechanism for the composites during stretching, (f) SEM of the composites.

Subsequently, the mechanical properties could be further improved by constructing the second cross-linked network based on the coordination interaction. The mechanical properties of the composites were gradually improved by increasing Fe^{3+} content. Interestingly, the tensile behavior of the composites changed dramatically when the Fe^{3+} content reached 2 phr. For example, PA0.5F2 showed the highest tensile strength and tensile toughness of 16.99 MPa and 28.43 MJ/m^3 (Figure S9), which were 6.56 times and 2.32 times that of the ENR/PCL simple blend. The outstanding reinforcing efficiency of the coordination cross-linked network is mainly due to the improved energy dissipation,[33] which will be further discussed in the subsequent section. When further increasing the Fe^{3+} content, a yield point could be found in the stress-strain curve of PA0.5F3, which was accompanied by the obvious improvement in the stress at 100 % strain and *E'* (Figure S10). A cross-linked network with a fairly high cross-link density (Figure 3b) would cause the rigidification of the composites; thus, PA0.5F3 fractured quickly with the lowest elongation at break of 250%. Overall, PA0.5F2 exhibited better comprehensive mechanical properties, as it possesses a decent tensile strength without sacrificing its elasticity. The mechanical properties of the ENR/PCL/PA/$FeCl_3$ composites exceed those of other reported ENR-based composites[8-11,33,42-44] (Figure 4b).

To understand the energy dissipation mechanism of the coordination cross-linked network, cyclic tensile tests were carried out on the samples of PA0.5F0, PA0.5F2, and PA0.5F3, as shown in Figure 4c. The energy dissipation capability of the composites can be characterized through the hysteresis loop enclosed by the loading-unloading curve, in which the hysteresis energy is obtained by calculating the hysteresis loop area, as depicted in Figure 4d. It can be found that the hysteresis energy increased with increasing Fe^{3+} content, disclosing that an impeccable second cross-linked network based on a coordination complex was formed to promote energy dissipation. On the one hand, the cross-link density of the composite was improved through the introduction of the coordination cross-linked network, resulting in a rigid network that resists the destructive effects of external force. On the other hand, the Fe^{3+}-based coordination complex could act as a sacrificial component to dissipate energy more efficiently. When suffering external force, the coordination complex underwent reversible deformation and breaking-reformation processes, which could help dissipate energy and alleviate the stress concentration, preventing the premature failure of the covalent cross-linked

DOI: 10.1039/D5TA03812J

network (Figure 4e). Therefore, PA0.5F2 showed a hysteresis energy of 0.90 MJ/m^3, which was nearly 4.29 times that of PA0.5F0. When further increasing Fe^{3+} content, the coordination bonds may be aggregated to form aggregations[33], inducing the plastic deformation and the mechanical "tough-brittle" transition of ENR/PCL components.

The fractured surfaces of the stretched PA0.5F0, PA0.5F2, and PA0.5F3 were observed via SEM and shown in Figure 4f. As an elastomer with a single cross-linked network, PA0.5F0 would break quickly when the covalent cross-linked network fails, resulting in a relatively smooth fractured surface for PA0.5F0. However, a rough morphology could be found in the fractured surface of PA0.5F2, which was due to the Fe^{3+}-based coordination preventing the premature failure of the covalent cross-linked network. A dramatic change could be found in the fractured surface of PA0.5F3, in which many stretched elastic microfibrils and obvious plastic deformation were formed during stretching. Meanwhile, the morphology along the tensile direction was also observed. Similar to the fractured surfaces, a rough morphology could be observed in the homoaxial surface of the composites (PA0.5F2), which was considered the typical morphology of reinforced elastomers[31]. Furthermore, many obvious microfibrils with considerable length along the stretching direction could be found in PA0.5F3, providing the composites with enhanced modulus and improved tensile strength. Although this orientation of microfibrils could improve the tensile strength of PA0.5F3 to some extent, the mechanical "tough-brittle" transition would also deteriorate its elasticity (Figure 4a) and increase its residual strain (Figure 4c, Figure S11), which was contrary to our design target. Considering the best comprehensive mechanical properties of PA0.5F2, we will further explore its shape memory performance in the next section, aiming to design a composite with decent elasticity and shape memory properties.

3.3 Heat-triggered shape memory behavior of the composite

For the pure ENR, it exists in a rubbery state at room temperature and cannot maintain its temporary shape. For the pure PCL, it cannot be programmed to the temporary shape when heated to 60 ℃, as it will melt and its structure will be destroyed (Figure S12). Therefore, we envision designing ENR/PCL shape memory composites by combining their potential in fabricating SMPs. In the plastic/rubber system, the plastic component can act as net points to fix the temporary shape, while the rubber component provides a resilient force to drive the shape recovery process[45,46]. To provide visual cognition of the shape memory effect, specimens with different formulas were deformed into various shapes to observe their shape fixing and shape recovery processes. As shown in Figure 5a,

View Article Online
DOI: 10.1039/D5TA03812J

the ENR vulcanizate cured by 0.5 phr PA could not fix its temporary shape, as it was in a rubber-like state at room temperature. However, with the incorporation of PCL, the ENR/PCL elastomer (PA0.5F0) could fix the temporary shapes better, visually demonstrating the effect of PCL on the shape fixing behavior. Meanwhile, the shape recovery behavior of the ENR/PCL/PA/$FeCl_3$ composite was also evaluated and shown in Figure 5b. A butterfly-shaped and an eagle-shaped specimen could realize the opening of their wings through the shape recovery process, showcasing the excellent shape memory behavior of the composites.

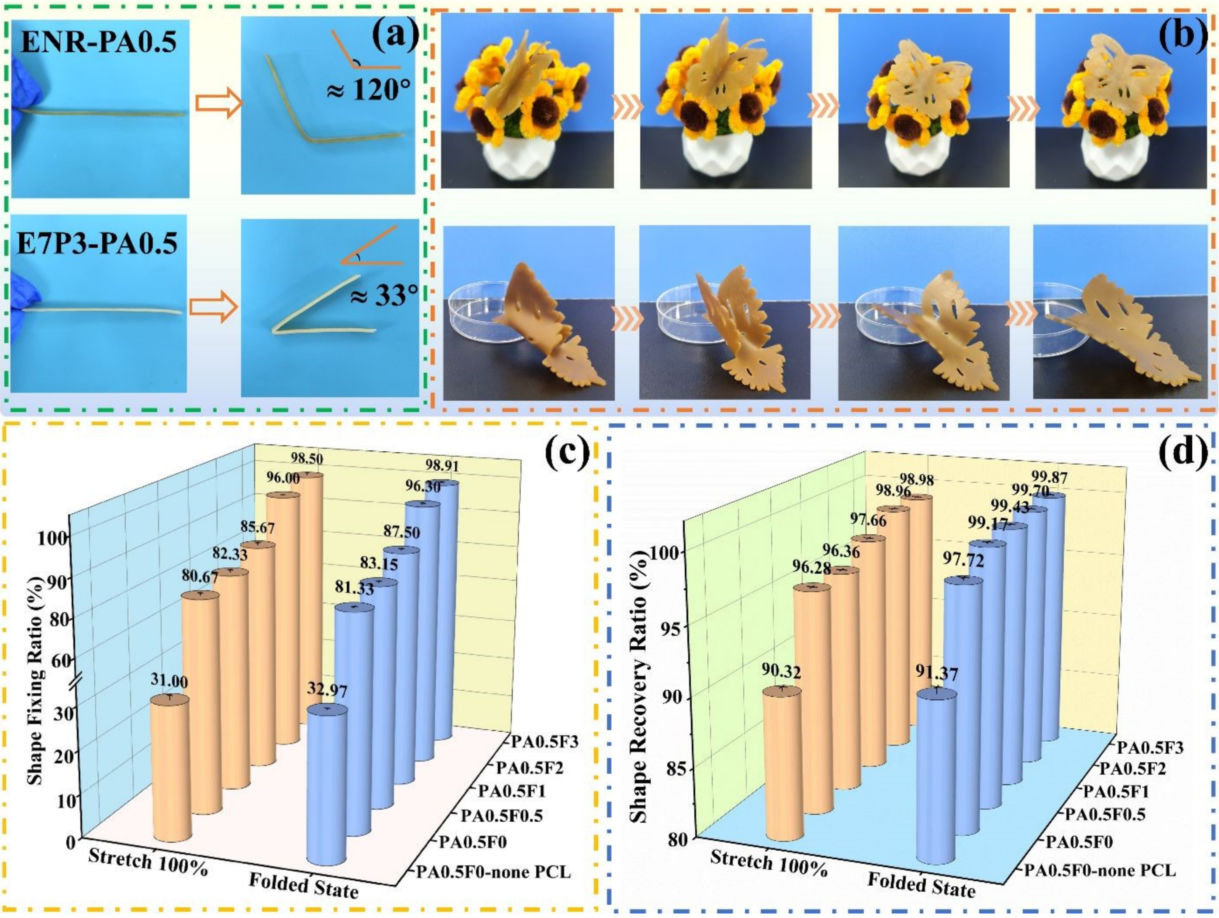

Figure 5. (a) Shape fixing behavior of the ENR/PA vulcanizate and ENR/PCL/PA elastomer, (b) shape recovery process of the ENR/PCL/PA/$FeCl_3$ composites, (c) shape fixing ratios and (d) shape recovery ratios of the ENR/PCL/PA/$FeCl_3$ composites.

The shape memory parameters, such as shape fixing ratio (R_f) and shape recovery ratio (R_r), were calculated according to our previous works, which are detailed in the *Supporting Information* (Figure S3). Since the PCL phase was in a glassy state at room temperature, it could act as net points to hold the temporary shape, thereby restricting the elastic retraction of deformed ENR chains. Therefore, the shape fixing effect was significantly enhanced with the incorporation of PCL (Figure S13). For example, the R_f value increased from 31.00% of ENR vulcanizate to 81.33% of PA0.5F0 (Figure 5c).

View Article Online
DOI: 10.1039/D5TA03812J

The shape fixing effect could be further improved by introducing Fe^{3+}. When adding 2 phr Fe^{3+}, the R_f value of PA0.5F2 reached 96.30%, which was because the coordinate bonds could act as a second type of net point to restrict the mobility of ENR chains.

The ENR/PCL simple blends showed an inferior shape recovery effect with R_r of 83.33% (Figure S13), as the unvulcanized ENR relaxed during deformation and was insufficient to drive the recovery of the original shape. In comparison, the ENR/PCL elastomers demonstrated excellent shape recovery performance, with R_r exceeding 95% (Figure 5d).

The ENR chains were cured by PA to form a three-dimensional cross-linked network, preventing stress relaxation during shape fixing, thus providing enough resilience to drive shape recovery when heated to its transformation temperature. With the incorporation of Fe^{3+}, a dual cross-linked network consisting of phosphate esters and coordination bonds was constructed in the matrix, further improving the R_r value of ENR/PCL/Fe^{3+} composites. The composites maintained relatively high R_f and R_r with increasing strains, with all samples showing R_f over 95%, disclosing the stability in the shape recovery effect and a broad response strain range of the composites (Figure S14).

3.4 Light-triggered shape memory behavior

The light-responsive capacity can be introduced into SMPs by integrating intrinsic light-responsive molecular units and incorporating photothermal agents[47-49]. Many studies have revealed that Fe^{3+}-based coordination compounds exhibit an excellent photothermal effect, which can be utilized as photothermal agents to enable the photothermal function of the composites[29,44,47,48]. We envision designing light-triggered SMPs by introducing the photothermal effect into the fabricated heat-triggered SMPs. The shape memory effect of this type of light-triggered SMP is intrinsically triggered by heat, which is provided by the photothermal effect[20,29]. Therefore, to visually evaluate the photothermal effect of the ENR/PCL/PA/$FeCl_3$ composites, a near-infrared light (NIR, 808 nm) was used to irradiate the composite sheets, and an infrared thermal imager recorded the surface temperatures (Figure S15). As shown in the infrared images (Figure 6a) and the summarized temperature curves (Figure 6b), PA0.5F0 showed small fluctuations in surface temperatures under NIR irradiation, caused by its inferior light absorption capacities (Figure S16). However, as the light absorption capacity was significantly improved by the formation of Fe^{3+}-based coordination compounds, the ENR/PCL/PA/$FeCl_3$ composites were noticeably heated by NIR, and their surface temperature increased with increasing Fe^{3+} content. The photothermal conversion could be regulated by adjusting the distances between the photosource and the target, which effectively altered the power

View Article Online
DOI: 10.1039/D5TA03812J

of NIR irradiation (Figure 6c). Meanwhile, the composites showed good reproducibility in photothermal conversion even after repeatedly switching NIR irradiation for several cycles.

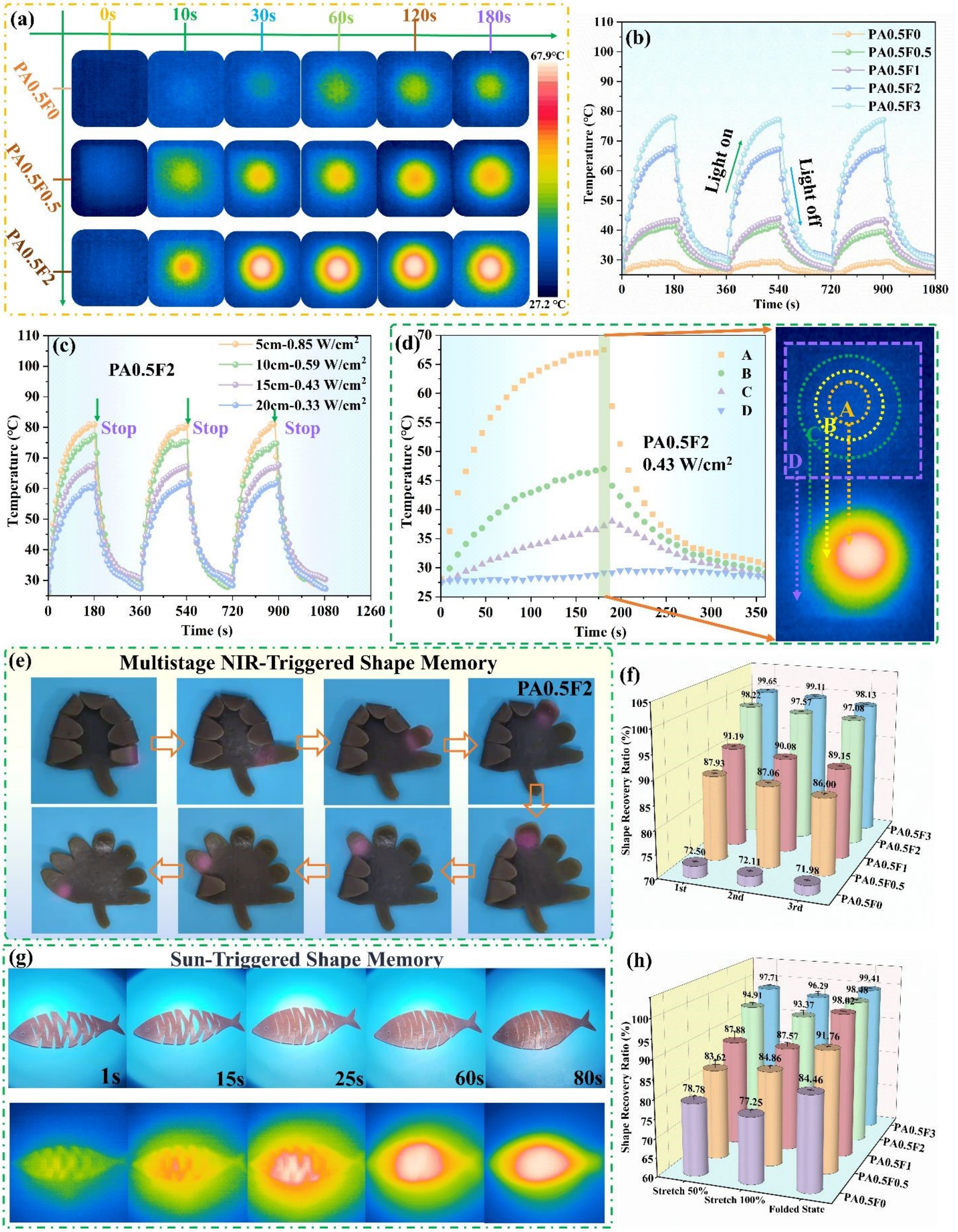

Figure 6. (a) the photothermal effect of the ENR/PCL/PA/FeCl$_3$ composites, (b) temperature-time curves of the composites under switching NIR laser irradiation (0.43 W/cm^2) for 3 cycles, (c) temperature-time curves of PA0.5F2 with different distances between NIR laser and the sample, (d)

View Article Online
DOI: 10.1039/D5TA03812J

temperature curves of the different spots of PA0.5F2, (e) multistage NIR-triggered shape memory behavior of PA0.5F2, (f) shape recovery ratio of the composites under NIR irradiation, (g) shape recovery process of PA0.5F2 under sunlight irradiation, (h) shape recovery ratio of the composites under sunlight irradiation.

In our previous work, we found that the photothermal effect of NIR irradiation could only be generated at the irradiating region[20,31]. Therefore, PA0.5F3 was taken as an example to record the temperatures of different spots under NIR irradiation. As shown in Figure 6d, the irradiated focus (spot A) could be heated to 67.90 ℃, while no obvious change in temperature could be found at spot C and spot D. The multistage shape recovery performance of the composites could be realized based on this characteristic. A ginkgo leaf-shaped specimen of PA0.5F2 was first folded at 60 ℃ and cooled to fix the temporary shape (Figure 6e, Movie S1). When the leaf was irradiated by NIR, it was heated to a temperature above the T_m of PCL to realize the blooming of this leaf, while other leaves without irradiation could maintain their closed shape. Other leaves could bloom sequentially when independently irradiated by NIR, displaying the multistage shape memory behavior of the composites. As shown in Figure 6f, the shape recovery test of the composites under NIR irradiation was conducted, and the R_r values of the composites were calculated to evaluate the NIR-induced shape memory performance quantifiably. With the construction of the Fe^{3+}-based coordination compounds, the composites could be heated above the T_m of PCL quickly to achieve shape recovery, realizing the R_r values of more than 86.00%. The composites maintained a high R_r value as the number of shape recovery cycles increased. For example, PA0.5F2 showed an R_r of 97.08% even after the third shape recovery cycle, demonstrating good reproducibility in the NIR-induced shape memory behavior.

Similarly, the ENR/PCL/PA/$FeCl_3$ composites can also be indirectly heated by sunlight, which is beneficial for realizing the shape recovery behavior. As shown in Figure 6g, the composite sheet was custom-made as a fish and stretched to a temporary shape, and then the fish was heated by a sun simulator to induce shape recovery (Movie S2). The R_r values of the composites under sunlight irradiation were also calculated and shown in Figure 6h. It could be found that the tendency of the R_r values under sunlight was similar to the R_r values under NIR irradiation. PA0.5F2 showed an R_r of 93.57% under a stretched shape (100% strain) and 98.48% under a folded shape, demonstrating the outstanding light-induced shape memory behavior of the composites.

3.5 Photothermal performance and application in thermoelectric power generation

Solar energy is an inexhaustible and widely distributed source of clean energy, which can be used

View Article Online
DOI: 10.1039/D5TA03812J

through light-heat-electricity transformation, helping to reduce carbon emissions. Based on the preliminary exploration of the sunlight-induced shape memory performance, we assume that the ENR/PCL/PA/$FeCl_3$ composites can be further utilized to fabricate a photo-thermoelectric generator (PTEG). Firstly, the photothermal conversion performance of the composites under sunlight irradiation was investigated thoroughly. As shown in Figure 7a, the photothermal effect was evaluated by a testing device including a sun simulator and an infrared thermal imager. Compared to the small fluctuations of PA0.5F0, the ENR/PCL/PA/$FeCl_3$ composites could be remarkably heated by sunlight, and their surface temperature could be improved by increasing the Fe^{3+} content (Figure 7b). For example, the surface temperature of PA0.5F2 increased rapidly to ~87.40 ℃ in only 90 s. Meanwhile, the repeated temperature curves of PA0.5F2 were recorded by switching the sun simulator for 30 cycles. As shown in Figure S17, the composite exhibited excellent repeatability in the photothermal effect, which would provide important support for the repetitive behavior of thermoelectric power generation and light-triggered shape memory behavior. The maximum surface temperature of the composites could also be regulated by adjusting the power density of the sun simulator. As shown in Figure 7c, the maximum surface temperature of PA0.5F2 increased from 68.4 ℃ to 109.4 ℃ as the sun simulator power density increased from 0.10 to 0.30 W/cm^2, while the composites could maintain excellent thermal stability (Figure S18).

Based on the outstanding photothermal effect of the ENR/PCL/PA/$FeCl_3$ composites, a PTEG integrated with a Seebeck thermoelectric generator, a heat sink, and a PA0.5F2 film was designed to explore the potential application in photo-thermoelectric conversion, as shown in Figure 7d. When exposed to the sun simulator, PA0.5F2 film quickly generated heat and transferred it to the upper surface of the thermoelectric generator, leading to a temperature difference between the different sides of the generator. Therefore, an open circuit voltage was generated based on the Seebeck effect (Figure 7e). The output voltage of the PTEG system increased rapidly to reach its stable value of ~0.41 V under exposure to sun irradiation (0.20 W/cm^2). Similar to the repeatability of the temperature curve (Figure 7b), the output voltage maintained good reproducibility after 5 cycles of switching sun irradiation (Figure 7f). Meanwhile, the output voltage upon sun irradiation could be controlled by varying the power of the sun simulator (Figure 7g). The above results disclosed a highly efficient photo-thermal-electrical conversion system based on the ENR/PCL/PA/$FeCl_3$ composites. Subsequently, the fabricated photo-thermoelectric generator was utilized to rotate a small fan (Figure 7h, Movie S3), which could be applied to improve the working environment for couriers (Figure 7i).

View Article Online
DOI: 10.1039/D5TA03812J

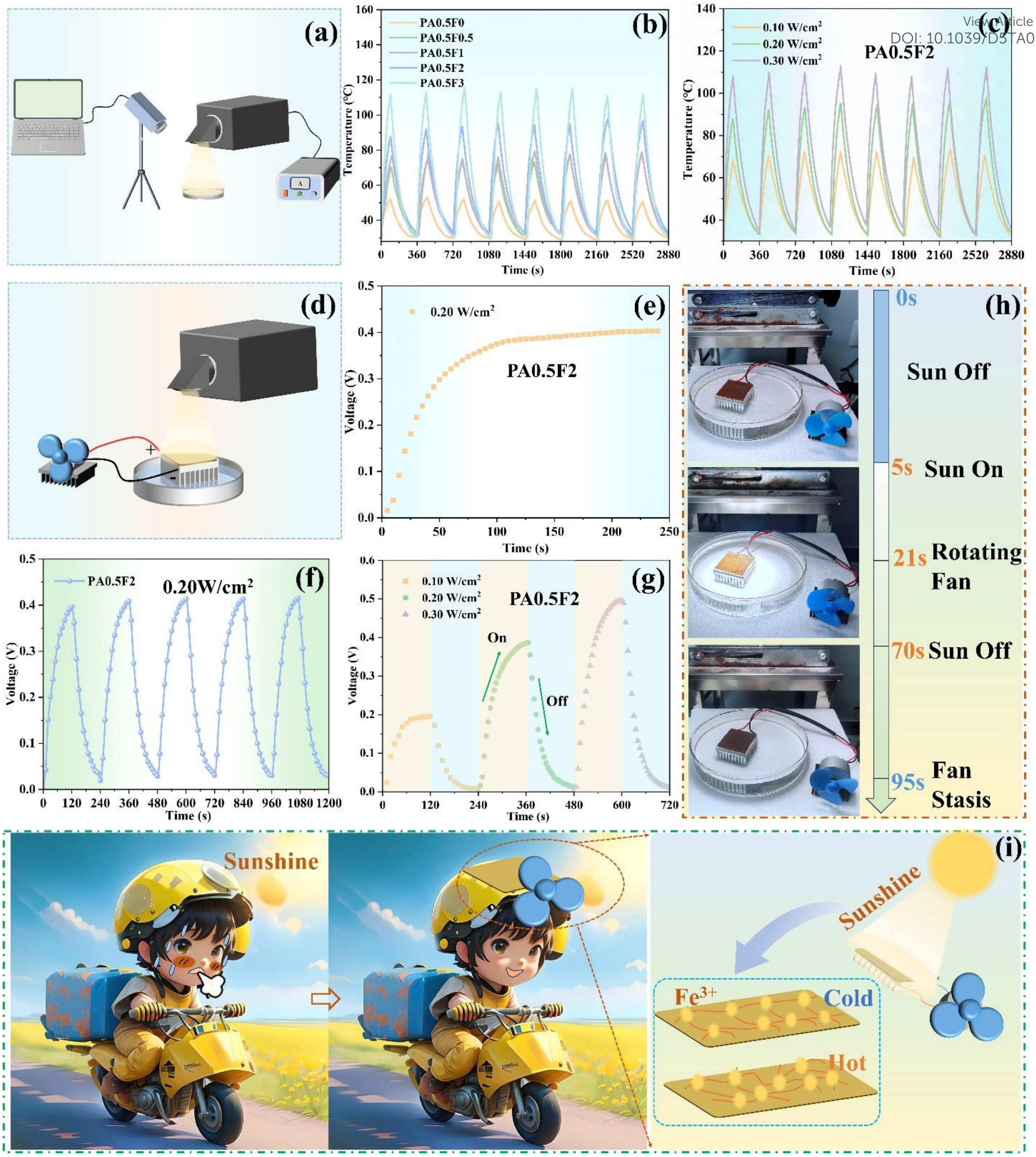

Figure 7. (a) Experimental setup of the sun simulator, (b) temperature-time curves of the composites under switching sun simulator (0.20 W/cm^2) for 8 cycles, (c) temperature-time curves of the composites with different laser powers, (d) experimental setup of a photo-thermoelectric generator, (e) voltage of PA0.5F2 generated from the irradiation of the sun simulator, (f) cycling performance in terms of output voltage, (g) voltage upon sun simulator irradiation with different powers, (h) application of a photo-thermoelectric generator, (i) the delivery man's helmet with photo-thermoelectric generator.

View Article Online
DOI: 10.1039/D5TA03812J

Conclusion

In summary, we prepared rubber composites with tunable mechanical properties, photothermal capability, and multi-stimuli-responsive shape memory performance by introducing a plastic component and constructing a dual cross-linked network. PA was utilized to cure ENR via the ring-opening reaction between phosphate groups and epoxy groups, while Fe^{3+} was introduced into the matrix to construct a second cross-linked network based on the coordination interaction between Fe^{3+} and oxygen-containing groups of ENR. The coordination cross-linked network could serve as a sacrificial element to significantly dissipate energy, remarkably improving the mechanical properties. The resulting composites showed an enhanced tensile strength of 16.99 MPa and a tensile toughness of 28.43 MJ/m^3, which is 48.54 times and 4.44 times greater than that of the pure ENR, respectively. PCL was introduced into the ENR matrix and acted as net points to regulate the shape fixing behavior of ENR, while the dual cross-linked network provided strong resilience to trigger the shape recovery process, endowing the composites with an outstanding shape fixing ratio of 98.91% and shape recovery ratios of 99.87%. Furthermore, the Fe^{3+}-based coordination complex was available as a photothermal agent to realize the light-induced shape memory behavior and thermoelectric power generation under NIR or sun irradiation. The fabricated rubber composites showed enormous potential in harvesting sunlight for outdoor portable power generation and also brought inspiration for the development of stimuli-responsive sensors.

Acknowledgment

This work was supported by Guangdong Basic and Applied Basic Research Foundation (2024A1515011787, 2023A1515110321), Youth Innovative Talents Project of Education Department of Guangdong Province (2023KQNCX086), 2023 Jiangmen Basic and Theoretical Science Research Science and Technology Plan Project (2023JC01017).

Supporting Information

Supporting tables, and figures are available free of charge on the Publications website.

Reference

1 M. Su, Y. Song, *Chem. Rev.*, 2022, **122**, 5144-5164.

2 B.O. Altas, C. Goktas, G. Topcu, N. Aydogan, *ACS Appl. Mater. Interfaces*, 2024, **16**, 15533-15547.

3 X. Wang, J. Xu, Y. Zhang, T. Wang, Q. Wang, S. Li, Z. Yang, X. Zhang, *Nat. Commun.*, 2023,

View Article Online
DOI: 10.1039/D5TA03812J

14, 4712.

4 J. Xu, M. Shao, T. Chen, S. Li, Y. Zhang, Z. Yang, N. Zhang, X. Zhang, Q. Wang, T. Wang, *Adv. Sci.*, 2024, **11**, 2406193.

5 X. Li, B. Zhan, X. Wang, Y. Liu, Y. Liu, J. Leng, *Compos. Sci. Technol.*, 2024, **247**, 110398.

6 J. Xu, M. Shao, X. Wang, T. Chen, S. Li, X. Zhang, T. Wang, Y. Zhang, Z. Yang, Q. Wang, *Adv. Mater.*, 2024, **36**, 2311992.

7 J.C. Kim, Y.W. Chang, M. Sabzi, *Eur. Polym. J.*, 2021, **152**, 110488.

8 L. Kong, Y. Yang, Z. Lin, B. Huang, L. Liao, Y. Wang, C. Xu, Chem. Eng. J., 2024, **479**, 147624.

9 Y. Wu, C. Yan, Y. Wang, C. Gao, Y Liu, *Int. J. Biol. Macromol.*, 2021, **184**, 9-19.

10 S. Xu, Q. Jia, K. Zhang, C. Lu, C. Wang, J. Wang, Q. Yong, F. Chu, *Int. J. Biol. Macromol.*, 2024, **268**, 131946.

11 J. Huang, Z. Gong, Y. Chen, Polymer, 2022, 242, 124569.

12 J. Xu, X. Wang, X. Zhang, Y. Zhang, Z. Yang, S. Li, L. Tao, Q. Wang, T. Wang, *Chem. Eng. J.*, 2023, **451**, 138673.

13 H. Tong, Y. Chen, Y. Weng, S. Zhang, *ACS Sustainable Chem. Eng.*, 2022, **10**, 7942-7953.

14 T. Shou, Q. Dong, D. Yin, S. Hu, X. Zhao, L. Zhang, *Compos. Part B-Eng.*, 2024, **276**, 111363.

15 M. Lira, R. Cunha, P. Agrawal, G. Brito, T. Mélo, *Macromolecules*, 2024, **57**, 7315-7330.

16 Q. Yu, Q. Fan, W. Chen, Y. Chen, C. Du, G. Fang, Y. Wu, H. Liu, *Compos. Part B-Eng.*, 2024, **498**, 155410.

17 Y. Ma, Ji. Meng, L. Xia, *Eur. Polym. J.*, 2022, **179**, 111530.

18 H. Kang, Y. Cui, X. Li, J. Hu, H. Ni, D. Li, L. Li, Q. Fang, J. Zhang, *Ind. Eng. Chem. Res.*, 2024, **63**, 11218-11229.

19 M. Xu, Y. Zong, C. Zong, *Polymer*, 2023, **285**, 126328.

20 J. Huang, H. Wu, X. Wang, L. Tan, W. Xu, Q. Wang, Y. Liang, H. Yu, Z. Liu, B. Xu, S. Xiao, *Int. J. Biol. Macromol.*, 2024, **282**, 137173.

21 J. Huang, J. Fan, L. Cao, C. Xu, Y. Chen, *Chem. Eng. J.*, 2020, **385**, 123828.

22 E. Su, G. Bayazit, S. Ide, O. Okay, *Eur. Polym. J.*, 2022, **168**, 111098.

23 C. Li, X. Yang, Y. Wang, J. Liu, X. Zhang, *Adv. Funct. Mater.* 2024, **34**, 2410659.

24 C. Lin, X. Xin, L. Tian, D. Zhang, L. Liu, Y. Liu, J. Leng, *Compos. Part B-Eng.*, 2024, **274**, 111257.

25 R. Hua, F. Zhang, L. Luo, L. Wang, Y. Liu, J. Leng, *Chem. Eng. J.*, 2024, **489**, 150956.

View Article Online
DOI: 10.1039/D5TA03812J

26 R. Zhao, S. Kang, C. Wu, Z. Cheng, Z. Xie, Y. Liu, D. Zhang, *Adv. Sci.*, **2023**, 10, 2205428.

27 G. Chen, B. Jin, Q. Zhao, T. Xie, *J. Mater. Chem. A*, 2021, **9**, 6827-6830.

28 Z. Huang, Z. Wu, C. Li, X. Li, X. Yang, X. Qiu, Y. Wang, Y. Miao, X. Zhang, *Adv. Mater.* 2025, **37**, 2413194.

29 J. Huang, J. Zhang, X. Wang, L. Tan, Q. Wang, B. Xu, W. Xu, *Chem. Eng. J.*, 2025, **515**, 163369.

30 M. Wu, T. Luo, J. Lu, Y. Wang, B. Lin, C. Xu, *Compos. Sci. Technol.* 2023, 235, 109966.

31 J. Huang, X. Wang, H. Wu, S. Xiao, Y. Liang, H. Yu, B. Xu, W. Xu, L. Tan, *Chem. Eng. J.*, 2024, **490**, 151516.

32 E. Ducrot, Y. Chen, M. Bulters, R.P. Sijbesma, C. Creton, *Science*, 2014, **344**, 186-189.

33 S. Yu, Z. Tang, D. Wang, B. Guo, L. Zhang, *Macromolecules*, 2024, **57**, 10120-10129.

34 S. Wang, Z. Tang, Y. Xiao, D. Wang, B. Guo, L. Zhang, *Compos. Sci. Technol.*, 2025, **260**,110964.

35 J. Huang, H. Wu, X. Wang, H. Yu, S. Xiao, L. Tan, B. Xu, *Polymer*, 2024, **297**, 126852.

36 J. Lu, Z. Li, J. Chen, S. Li, J. He, S. Gu, B. Liu, L. Chen, Y. Wang, *Research*, 2022, 9846940.

37 X. Yang, Y. Guo, L. Kong, J. Lu, B. Lin, C. Xu, *Int. J. Biol. Macromol.*, 2023, 242, 124681.

38 Q. Guo, J. Cao, Y. Han, Y. Tang, X. Zhang, C. Lu, *Green Chem.* 2017, 19, 3418.

39 X. Zhang, Z. Tang, B. Guo, L. Zhang, *ACS Appl. Mater. Interfaces*, 2016, **8**, 32520-32527.

40 K. Buaksuntear, K. Panmanee, K. Wongphul, P. Lim-arun, S. Jansinak, D.U. Shah, W. Smitthipong, *Polymer* 2024, **291**, 126626.

41 Z. Li, H. Li, T. Xie, W. Gao, *ACS Appl. Polym. Mater.* 2024, **6**, 9685-9693.

42 L, Zhao, L. Liu, J. Gao, L. Zhang, *Polymer*, 2024, **311**, 127550.

43 T. Siriwas, S Pichaiyut, C. Nakason, *Ind. Crop. Prod.*, 2024, **219**, 119040.

44 J. Zhu, Y. Chen, P.C. Lee, S. Zhang, *J. Mater. Chem. A*, 2024, **12**, 30486-30497.

45 N. Lehman, L. Songtipya, J. Johns, K. Maliwankul, S.P. Voravuthikunchai, Y. Nakaramontri, K. Sengloyluan, E. Kalkornsurapranee, *Express Polym. Lett.* 2021, **15**, 28-38.

46 Y. Chang, J. Eom, J. Kim, H. Kim, D. Kim, *J. Ind. Eng. Chem.* 2010, **16**, 256-260.

47 C. Zhang, L. Huang, D.W. Sun, H. Pu, *J. Hazard. Mater.*, 2022, **426**, 127824.

48 H. Wang, X. Wen, K. Liu, Q. Liu, G. Hu, H. Liu, Y. She, R. Niu, T. Tang, J. Gong, *SusMat.* 2024, **4**, e242.

49 G. Fan, S. Wang, J. Jiang, Z. Liu, Z. Liu, G. Li, *Chem. Eng. J.*, 2022, **447**, 137534.

View Article Online
DOI: 10.1039/D5TA03812J

Data Availability Statement

Data available on request.

The data underlying this article will be shared on reasonable request to the corresponding author